

# Real2Sim2Real Transfer for Control of Cable-driven Robots via a Differentiable Physics Engine

Kun Wang<sup>1</sup>, William R. Johnson III<sup>2</sup>, Shiyang Lu<sup>1</sup>, Xiaonan Huang<sup>2</sup>,  
Joran Booth<sup>2</sup>, Rebecca Kramer-Bottiglio<sup>2</sup>, Mridul Aanjaneya<sup>1</sup>, and Kostas Bekris<sup>1</sup>

**Abstract**—Tensegrity robots, composed of rigid rods and flexible cables, exhibit high strength-to-weight ratios and extreme deformations, enabling them to navigate unstructured terrain and even survive harsh impacts. However, they are hard to control due to their high dimensionality, complex dynamics, and coupled architecture. Physics-based simulation is one avenue for developing locomotion policies that can then be transferred to real robots, but modeling tensegrity robots is a complex task, so simulations experience a substantial sim2real gap. To address this issue, this paper describes a Real2Sim2Real strategy for tensegrity robots. This strategy is based on a differential physics engine that can be trained given limited data from a real robot (i.e. offline measurements and one random trajectory) and achieve a high enough accuracy to discover transferable locomotion policies. Beyond the overall pipeline, key contributions of this work include computing non-zero gradients at contact points, a loss function, and a trajectory segmentation technique that avoid conflicts in gradient evaluation during training. The proposed pipeline is demonstrated and evaluated on a real 3-bar tensegrity robot.

## I. INTRODUCTION

Tensegrity robots are compliant systems composed of rigid struts (rods) and flexible elements (cables) connected to form a lightweight, deformable structure. Their natural compliance makes them adaptable and safe robots well-suited to applications like manipulation [1], locomotion [2], morphing airfoils [3], and spacecraft lander design [4]. At the same time, they are difficult to accurately model and control due to their high degrees of freedom and complex dynamics.

Simulators are important tools for developing locomotion policies for tensegrity robots [5]. Learning effective control policies for tensegrity robots is challenging with model-free solutions since they require a large amount of training data and collecting trajectories from tensegrities is time-consuming, cumbersome and expensive. Thus, a better alternative is to tune a dynamical model, or a tensegrity simulator [5], [6], [7], [8], [9], [10], of the system to minimize the difference between trajectories predicted by the model relative to those executed by a robot (henceforth referred to as the *ground-truth system*). This is a system identification problem, which is necessary before employing a model-based controller.

This work has been supported by NSF Robust Intelligence award 1956027. The opinions expressed here are those of the authors and do not reflect the positions of the sponsor. <sup>1</sup>Computer Science, Rutgers University, NJ 08901, USA. Email: {kun.wang2012, shiyang.lu, mridul.aanjaneya, kostas.bekris}@rutgers.edu. <sup>2</sup>Mech. Eng. & Material Sc., Yale University, New Haven, CT, USA. Email: {will.johnson, xiaonan.huang, joran.booth, rebecca.kramer}@yale.edu.

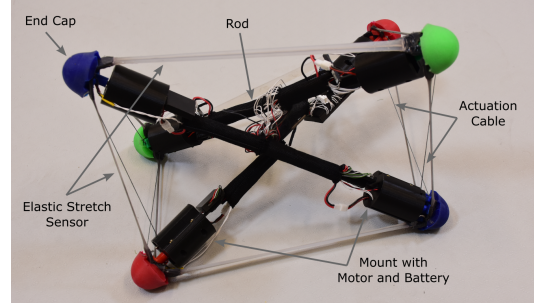


Fig. 1. The target experimental platform for this work: a three-bar prismatic tensegrity robot with three rods and nine stretch sensors attached on the end cap. Six short cables are contracted and extended by motors in the 3D-printed housings on each rod.

The reality gap is the main barrier that prevents successful policy transfer onto the real robot [11], [12]. To overcome this gap, researchers have applied many methods, including more realistic photos [12], differentiable rendering [13], accuracy evaluation of various simulators [14], adaptive domain randomization [15], [16], etc. The robot or the manipulated objects are rigid in most of these cases [17]. Compliant objects like springs and cables are less investigated, and their presence makes closing the sim2real gap more challenging. Recently, a Real2Sim2Real (R2S2R) framework was introduced for manipulating deformable cables [18]. Instead of manipulating the deformable objects, we focus on controlling deformable robots composed of soft materials.

In this paper, we introduce the first R2S2R pipeline for tensegrity robots and transfer the policy learned from a differentiable engine to three-bar tensegrity robot (Fig 1). The contributions of this paper can be summarized as follows:

- A novel method to compute non-zero gradients at contact points to enable efficient learning of contact parameters in the downstream optimization phase.
- A novel loss function and a trajectory segmentation strategy to avoid conflicts in gradient direction during system identification over long trajectories and under noisy observations. Since non-convex trajectories lead to gradients with opposite directions at different time steps, we segment the trajectory into convex segments to ensure the gradients agree on a common direction to perform gradient descent.
- A complete pipeline that closes the loop of identifying differentiable simulator parameters from real tensegrity robot trajectories, generating locomotion policies in the simulator, and transferring the policies back to execute on the real tensegrity robot.

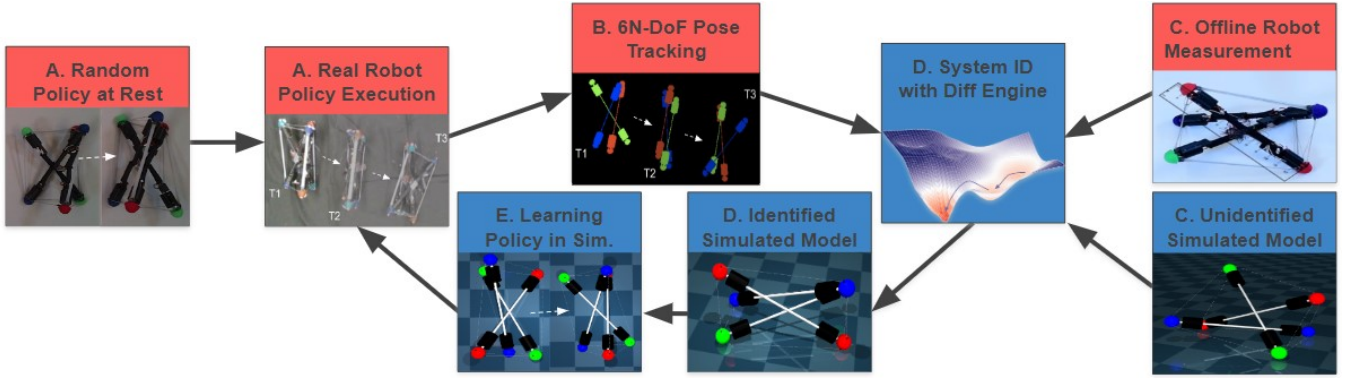


Fig. 2. R2S2R pipeline for policy transfer. A. We first generate a random policy and execute it on the real robot. B. We observe the execution using an external RGB-D sensor, which allows us to track the  $6N$ -dimensional pose of the robot, where  $N$  is the number of rigid elements of the robot. Given the pose tracking information and (C) offline robot measurements, e.g. mass, rod dimensions, etc., we (D) identify the internal parameters of a differentiable physics engine by gradient descent. Given the identified model, we generate a set of new locomotion policies and execute them on the real robot. Then the second iteration starts. The red blocks are done on the real robot and the blue blocks are on the simulation.

## II. RELATED WORKS

Differentiable physics is an active area of research, which has been applied to path optimization [19], training by image supervision [13], [20], soft object manipulation [21], [22], [23], [24], rigid robot control [25], [26], dynamics acceleration [27], soft robot control [28], [29], real time MPC [30], and quantum molecular control [31]. The differentiable engines specifically designed for tensegrity robots [32], [33], [34] provides successful Sim2Sim transfer but doesn't use real robot data.

Prior work on tensegrity locomotion [35], [36], [37] has achieved complex behaviors, on uneven terrain, using the NTRT simulator [5], which was manually tuned to match a real platform [38], [39]. Many of these approaches use reinforcement learning to learn policies given sparse inputs, which can be provided by onboard sensors [36] and aim to address the data requirements of RL approach [37], including by training in simulation. However, simulated locomotion is hard to replicate on a real platform, even after hand-tuning, which emphasizes the importance of learning a transferable policy, the focus of this work.

Sim2Real transfer has been applied widely to close the reality gap in autonomous underwater vehicles [40], drones [41], [42], muscles [43], quadruped robots [44], soft robots [45], [46], [47], and grasping manipulators [48]. Moreover, R2S2R transfer has been applied to estimate the dynamics of soft cables manipulated by rigid robots [18]. The current work is the first one mitigating the reality gap by showing R2S2R transfer on cable-driven soft robots.

## III. METHODS

The following discussion describes the components of the proposed R2S2R pipeline outlined in Fig. 2.

### A. Random Policy and Real World Execution

Usually the policy is a sequence of low level control signals, e.g. retracting, releasing or stalling the cables of a tensegrity robot, along with their duration of execution. However, this kind of policy is hard to transfer between two platforms because it requires strict agreement between them.

Instead, the policy here is defined as a list of robot cable lengths, which represent a series of target robot shapes. To transit between these high level shapes, a PID controller actuates the robot from current shape to next target shape by sending low level control signals to cables based on the feedback from the robot cable length sensors.

All policies start from the robot rest state, where the robot sits on the ground with six short cables fully extended. In the first iteration, a random policy is executed. In the following iterations, newly explored policies are executed.

### B. Data Collection

To collect the real robot trajectory, a pose tracking system is needed to get rod position and orientation at each time frame. However, the onboarding sensors based system [49] is hard to get global coordinates. The vision tracking system by fiducial markers [50] struggles by occlusions.

Until recently a tensegrity pose tracking method, that combines vision and on board sensors, is proposed [51] to overcome the above drawbacks. The 6-DoF poses of each rod is estimated given a multi-modal input sequence of RGB images, depth images, and measured cable lengths from on board elastic sensors. This method takes into account a variety of physical constraints and is able to perform accurate state estimation without the need of a complex motion capture system. RANSAC [52] is used for plane detection, so as to find contacts between endcaps and the ground, which is required for system identification. The sampled trajectory in first iteration is a random policy by retract and release each cable. The learned locomotion policies are executed to sample trajectory in following iterations.

### C. Offline Robot Measurements

Physical parameters inside a simulator, e.g. mass, radius, length, inertia, stiffness, friction coefficient, etc, are keys of modeling a real robot. But identifying all of them in one optimization is challenging due to uneven loss landscape. The more components in a robot, the more physical parameters in a simulator, and the harder to learn all of them.

To simplify the identification, we measure parameters that easy to access and hard to change, and set them as ground

truth in simulator. We measure the dimensions and mass of each component on a rod and apply these numbers into the simulation. The force versus displacement curve is measured for the passive tendons using a materials testing system (Instron 3345). The stiffness of the passive tendons is fit with a linear polynomial that is integrated into the simulator. The short cables are stiff and not elastic, which are represented as cables with a high stiffness coefficient in simulation.

#### D. System Identification

Differentiable physics engine often accompany with the gradient descent optimization to identify system parameters. Recently researchers have conducted identification of a differentiable physics engine [32], [33], [34] from a target simulator. However, the real tensegrity robot has not been taken as the target platform.

Still benefiting from the gradient descent, a real world 3 bar tensegrity, as shown in Fig. 1, is set to the target platform where the ground truth data are collected from. We identify the parameters that related to the environment and hard to measure, e.g. the motor speed, which is related to the battery level, and friction, which is determined by the ground material.

**Detecting Unobserved Parameters** The collected data only have partial robot observation. Some parameters, e.g. the cable attachment points, are not observed on real robot, but are crucial for tensegrity simulation. Previous tensegrity simulator, e.g. NTRT [5], attaches a cable on the rod ends, which simplified modeling process. However, the simulated robot may be stuck in a dead end state, which collapses onto the ground and can't recover back to the rest state, because all actuation cables are on the same surface, as shown in Figure 3 (Left), although the real robot never do.

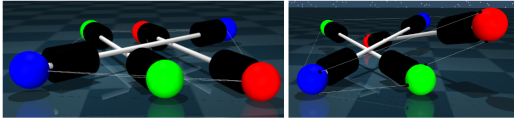


Fig. 3. (Left) After certain controls, the robot collapses onto the ground if all cables are attached to the end of the rods. (Right) With same controls, the robot doesn't collapse if all cables are attached on the surface of the end caps.

Instead, we put the cable attachment points on the surface of the end caps. This setup prevents the collapsing and results a more stable simulation, Figure 3 (Right), which allows more opportunity in policy exploration. Note that these attachment points are not available in the observations. We implement a heuristic to infer these attaching positions.

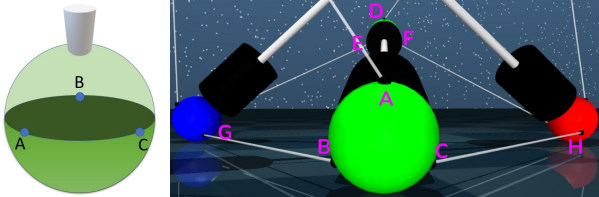


Fig. 4. Cable attachment points on end caps at rest state

The attachment points computation heuristic is inspired from the robot symmetry property. Each rod has 6 attachment points, which are distributed symmetrically and evenly on

two end caps. Since points are placed every  $2\pi/3$  on the disk that perpendicular to the rod, we can infer other 5 point positions once we get only one of them. At the robot rest state, one rod is in the center and other two rods are on the side as shown in Fig. 4. We first get compute  $A$  directly which is on top of the end cap. Then  $B, C, D, E, F$  can be inferred from it.  $G, H$  are closest to  $B, C$ . Then all rest points can be inferred.

**Initial State Alignment** Before each execution, the real robot resets itself to rest state. We reset the simulator also to align the initial state, e.g. position and orientation, same to the real robot. It is better to reduce the initial state difference since any small error in early stage will accumulate to large one in later stage during a open loop policy execution.

We align the real robot and the simulator by the collected data at  $t = 0$ , i.e. the initial positions of all end caps. The estimated end cap positions may be above the ground, as shown in Fig. 5 (left), directly applying them into the simulator will cause instabilities, because of the gravity and cable forces. To stabilize the robot, we compute the cables length by the connected end cap positions and initialize the simulator by both cable lengths and end cap positions. The gravity would drag the robot onto the ground, then the ground reaction and friction will stabilize the robot as shown in Figure 5 right.

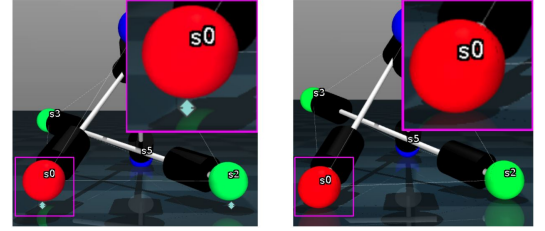


Fig. 5. (Left) The robot with estimated pose has gaps between the end caps and the ground. (Right) With gravity, the end caps touch down the ground without gaps.

#### Contact Gradients via the "Detachment" Approach

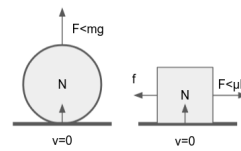


Fig. 6. (Left) Increasing  $F$  from zero to  $mg$  would reduce  $N$  equally resulting not change in velocity  $v = 0$ . (Right) Increasing  $F$  from zero to  $\mu N$  would increase the opposite static friction  $f$  and the velocity is still zero.

Previous works [53] have observed zero gradient issue for clamping contacts, where the perturbation in the control force of linear actuator will be met with an exactly offsetting contact force to ensure that the relative velocity between the actuated object and the ground remains zero. Figure 6 shows two cases of zero gradient under clamping contact, where the actuation forces  $F$  on the object are not enough to overcome the gravity or the friction. Gradients of loss function will be zeroed out by  $\partial v / \partial F = 0$ .

We propose a 'detach' method to get nonzero gradient. Since the passive forces like restitution and friction generates equal gradients on the opposite direction, gradients of these passive forces should not be backpropagated. The detach() function [54] returns a new tensor detached from the computational graph which truncate gradient propagation path.

We propose a 'detach' method to get nonzero gradient. Since the passive forces like restitution and friction generates equal gradients on the opposite direction, gradients of these passive forces should not be backpropagated. The detach() function [54] returns a new tensor detached from the computational graph which truncate gradient propagation path.



Detach method can be applied to learn restitution  $e$  and  $F$  in Figure 6 left, which is shown in Algorithm 1.  $\Delta v$  and  $\Delta x$  are detached to stop passive force gradient passing.

---

**Algorithm 1** Detach Method in Restitution Computation

---

```

 $v'_{t+1} = v_t - g\Delta t + F/m\Delta t$ 
 $\Delta v = -(1 + e)v'_{t+1}.detach()$ 
 $v_{t+1} = v'_{t+1} + \Delta v$ 
if  $x_t < ground$  then
     $\Delta x = ground - x_t$ 
     $x_{t+1} = x_t + v_{t+1}\Delta t + \Delta x.detach()$ 
else
     $x_{t+1} = x_t + v_{t+1}\Delta t$ 
end if

```

---

The detach method can also applied to friction learning which is listed in appendix.

**Identifying Appropriate Loss Function** The identification with long trajectory is difficult due the observation noise and non convex loss landscape.

a) *Noisy Observations*: The observations noise from the point clouds and cable length sensors may harm the identification process. As shown in Fig. 7, the later observations are preferable to reduce the fitting error.

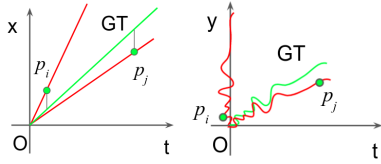


Fig. 7. Fitting the ground truth line (green) with two noisy observations,  $p_i$  and  $p_j$ . Although same sensing error are with  $p_i$  and  $p_j$ . The fitted line (red) by  $p_j$  is better than that by  $p_i$ .  $x = vt$  is a linear function (Left).  $y = f(t)$  is a non-convex function (Right).

b) *Contradicted Gradient Direction*: The loss landscape may be non convex due to contradictions in gradient direction, which stops the optimal optimization. As shown in Fig. 8, three losses yield opposite gradient directions.

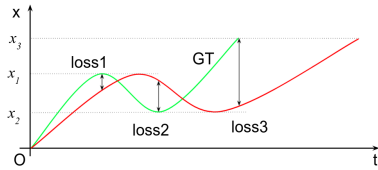


Fig. 8. The ground truth trajectory (green) includes three targets,  $x_1$ ,  $x_2$  and  $x_3$ . The unidentified engine has lower speed and takes longer time to reach them (red). Three losses are computed at these targets. The loss1 and loss3 provide gradients to pull up the red line, however, the loss2 drags it down.

Multiple-shooting (MS) has been applied to system identification with long trajectories recently [55]. However, MS needs full observation of robot to initialize the simulator. The defects may lead to contradicted gradient direction. How to select the window size is yet to be solved.

We introduced the Key Frame Loss (KFL), which split the trajectory to a list of convex subsets by the unidirectional control intervals, and only last step loss is considered in each subset. Four main differences comparing to MS are: 1) our system only has partial observation: we only know the end

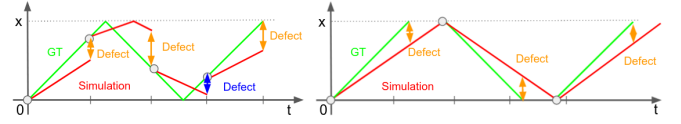


Fig. 9. (Left) The multiple-shooting method needs full observation at each time step. Thus simulator can align with ground truth at intermediate time steps, then execute length of a time window and compute the defects between ground truth and simulator. The window size is empirical and the defects may provide contradicted gradient directions. (Right) Our KFL method only needs partial observations at each time step. The trajectory is split to segments based on the unidirectional control intervals. The time frame at the end of control signal is the key frame where the loss of defects is computed. The window size is same to the control interval and the defects provide consistent gradient directions.

cap positions, without velocities.2) we can't recover simulator from the partial observed state, which has no velocities. 3) various sensing frequency: the observation sensing frequency is not constant. 4) the shooting time window size is not fixed. The comparison between MS and KFL is shown in Figure 9.

### E. Hybrid Control via Symmetry Reduction

Policy searching on a tensegrity robot is hard because of the combinatorial explosion of the high DoFs and high dimension state space. Symmetry reduction has been developed to 6 bar tensegrity robots [37], [56] to reduce the policy search space. However this idea has not been applied to the 3 bar tensegrity robots with 6 actuators. Here we combine the symmetry reduction into the hybrid control, where the high level planner gives next target state and the low level PID controller launches commands to control cable lengths.

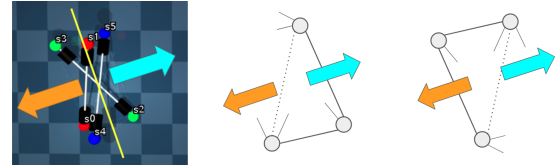


Fig. 10. (Left) The robot principle axis (yellow) is the average direction of the three rods. The forward direction (the cyan arrow pointing to the right) is to the front which is perpendicular to the axis, and the backward direction (the orange arrow pointing to the left) is to the opposite. (Right) Two robot poses, with different types of bottom triangles, are mapped after rotating  $\pi$  radius around the ground normal.

1) *State Volume Reduction*: We propose the relabeling mapping scheme based on the bottom triangle to reduce state volume. We set the robot state in Figure 10 (Left) as reference. We rotate the robot by its principle axis (the yellow line in ) with  $\pi/6$  interval and get two types of bottom triangles with opposite forward and backward direction after remapping. We rotate robot with second type triangle by  $\pi$  around the ground normal. After all rotations, we match the mapping by computing the closest end caps in the reference.

2) *Locomotion Gaits Generation*: Four locomotion policies are generated: forward flip, backward flip, clockwise turning and counter clockwise turning. Different loss functions are applied, e.g. CoM displacement, principle axis rotation angle. Starting from the rest state, we start a graph search where the node is robot state, represented by binary cable states (retracted or released), and the edge is cable controls, i.e. retract, release or stall. To reduce the search space, the depth is limited to 4 and the root node and leaf node are the same rest state, where all cables are released.

## IV. EXPERIMENTAL RESULTS

### A. Robot Platform Setup

A three-bar prismatic tensegrity robot is used to demonstrate this approach as shown in Figure 1. The tensegrity robot has a rod length of 36 cm, and it is driven by motors and cables. The six short tensegrity tendons (three on each side) are actuated by the motors while the three longer tendons in the middle are passive elastic elements. These passive tendons double as stretch sensors, and there are also six stretch sensors in parallel with the six actuated cables. The stretch sensors are made from a silicone elastomer (DragonSkin 20 or Eco-Flex 30; Smooth-On) and two encapsulated layers of a liquid metal paste made from eutectic gallium indium. The capacitance of the parallel plate capacitor formed by the two liquid metal layers varies linearly with the length of the tendon. Each sensor is calibrated individually by fitting a linear model to map capacitance measurements to corresponding lengths [57]. The stretch sensors are used for feedback control that closes the loop over the tendon length, allowing the robot to execute commanded gaits with high fidelity. The stretch sensors also aid in estimating the pose of the robot.

For the pose tracking system mentioned in section III-B, the color and depth image sequences are collected by an RGB-D camera (Intel Realsense L515) at 720p resolution.

As explained in section III-C, we measure the mass and dimensions of the rods and compute their inertia, which are listed in Table I. We apply a tensile test on the passive long cables to compute its stiffness (Figure 11). These numbers are applied to initialize simulator parameters.

TABLE I  
MEASURED PHYSICAL PARAMETERS

end cap	mass	10.5 g
	radius	17.5 mm
rod	mass	3.8 g
	radius	1.6 mm
	length	325 mm
mount with motor and battery	mass	35.3 g
	radius	17.5 mm
	length	45 mm
	low end to rod center	95 mm

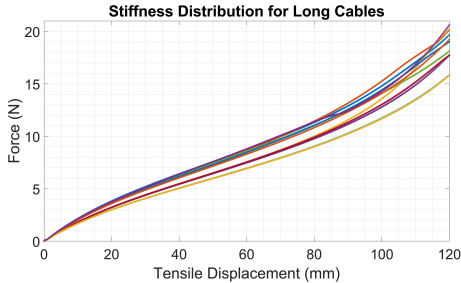


Fig. 11. A tensile test was performed on a batch of 11 long cables. A polynomial was fit to each sample's stiffness curve, and the average of these models was used in the simulator.

### B. System Identification with Synthetic Trajectories

To get rid of the effects of the real world observation noise, we evaluate the section III-D by a system identification experiment with synthetic trajectories.

We design three loss functions to show why we design the key frame loss: 1) average defects of all time steps (*All Step*) observations in each window; 2) average defects of the last time step (*Last Step*) observations in each window; 3) Our method (Ours) with Key Frame Loss, which average defects of last time step observations in each window and detach the observations between each window. Differences of these three methods are shown in Figure 12.

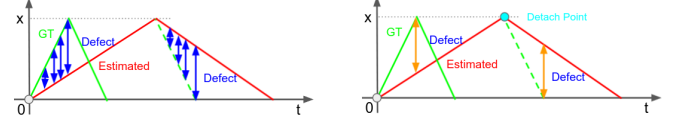


Fig. 12. A trajectory starts from origin, moves to  $x$ , and back to origin, and it can be split into two windows, the ground truth trajectory (green) takes less time than the estimated trajectory (red). The second window of ground truth trajectory is shifted to the right to compute defects. The All Step loss function is to average defects of all time steps positions in each window (Left). The Last Step loss function only average the last step position difference (Right). Our method (KFL) also detaches [54] the system state at the transition point (cyan) of two windows.

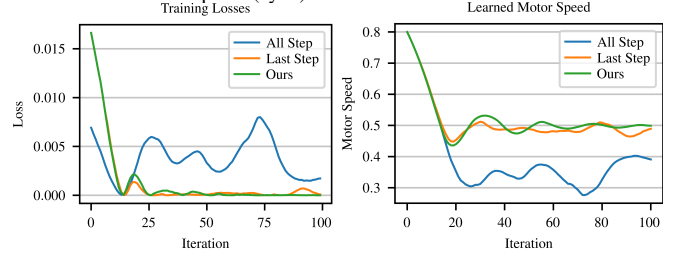


Fig. 13. To identify the motor speed parameter, we apply gradient decent with three different loss functions: naive loss by all time step defects (blue); the key frame loss by last time step defects (orange), and our KFL loss with state detachment (green). The KFL loss + detachment has better and faster convergence rate.

The task is to identify the motor speed. One synthetic trajectory that set motor speed to 0.5 is used as ground truth. The defects are end cap positions differences. An Adam optimizer with learning rate 0.1 is applied. Figure 13 shows that our method could converge fast and stable to the ground truth value. However, the other two methods can't converge smoothly even with multiple windows. It shows that a loss considering all time steps performs worse and detaching [54] the system states is necessary to stop the gradient propagation between windows.

### C. R2S2R Pipeline End-to-End Evaluation

The whole R2S2R pipeline is evaluated on the 3 bar tensegrity robot. We also iterate the pipeline cycle twice to show the continuous improvement.

In the *first* iteration, we sample a simple trajectory with random controls, identify the system, and then generate new polices. We generate four polices from the robot rest state: forward, backward and clockwise, counter clockwise turning. We mapped these policies to long trajectories by open loop symmetry reduction control. We execute the the controls both in simulation and real robot. In the *second* iteration, we reidentify the system with these real robot trajectories, and execute them again in simulation. The trajectories in simulation and real robot are plotted in Figure 14 and their

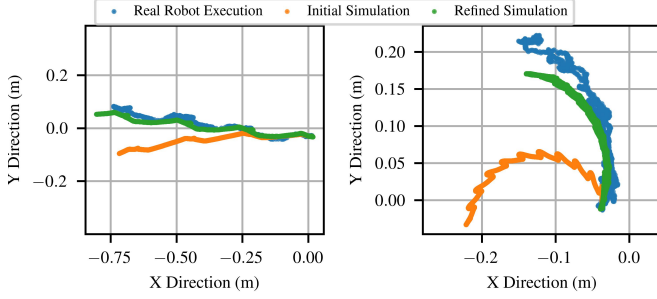


Fig. 14. The trajectory comparison in simulation and real world. All trajectory starts around (0, 0). These open-loop controlled trajectories are generated by basic policies: forward, backward, clockwise, counter-clockwise turning in symmetric reduction frames. First, we identify the simulator with a random trajectory and generate open-loop controlled trajectories. Second, we execute these controls on the real robot, sample the trajectories and refine the simulator. A straight line trajectory by executing consecutive forward and backward policy in symmetric reduction frame (Left). A curve trajectory by executing counter clockwise turning policy (Right).

TABLE II

LONG TRAJECTORY WITH OPEN LOOP CONTROL

	Center of Mass (m)		Orientation (radian)	
	Straight	Curve	Straight	Curve
Initial Simulation	[-0.72, -0.1]	[-0.22, -0.02]	0.23	2.54
Real Robot Execution	[-0.74, 0.08]	[-0.13, 0.22]	-0.23	1.78
Refined Simulation	[-0.8, 0.05]	[-0.1, 0.16]	-0.16	1.60
Initial Error	0.18	0.26	0.46	0.76
Refined Error	0.07	0.06	0.07	0.18

metrics are listed in the table II. The simulation trajectory is more close to the real robot trajectory after 2nd iteration. The error of turning trajectories are larger because the friction of the real environment is not uniform. The ground is a cloth and the crawling of a turning robot causes wrinkles.

#### D. Evaluation of Components

We design toy problems to evaluate our detach method and Key Frame Loss (KFL). Mean Square Error (MSE) and Adam optimizer are applied. The learning rate is 0.1.

1) *Contact Gradients with/without "Detach"*: First we test the trajectory optimization problem from [53], a drone taking-off from the ground and reaching a fixed height at  $t = 500$ , to evaluate the Algorithm 1. The loss is the MSE of drone height  $\hat{x}$  and target height  $x$ . The ground truth  $x = 10m$ .

The clamping contact between drone and ground causes zero gradients and make no progress in optimization, because the passive contact generates an opposite equal gradient to  $F$ . After detaching the contact velocity impulse  $\Delta v$  and position impulse  $\Delta x$  from computation graph in Algorithm 1, the correct gradient keeps increasing  $F$  even if there is no change in loss for the first 100 iterations (Figure 15).

#### 2) *SysID with/without KFL*:

We design another trajectory optimization problem, driving a car back and forth between A and B, to evaluate the KFL. We want to find the correct  $v$  to reach B at  $t = 100$ , back to A at  $t = 200$ , and back to B again at  $t = 300$ . The ground truth  $v = 1m/s$ .

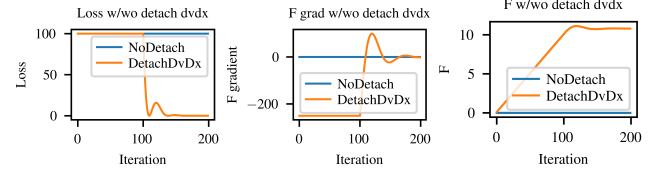


Fig. 15. We train a drone to lift off the ground to evaluate our "Detaching" method. Loss is the MSE of the distance from drone  $\hat{x}$  to target  $x$  at  $t = 500$ . The drone is initialized resting on the ground. The gradient  $\frac{\partial \hat{x}}{\partial F}$  is zero with clamping contact. However, after detaching the contact response  $\Delta v(dv)$  from computation graph, the correct gradient on  $F$  can guide the optimizer to increase  $F$  and reach the target.

We compare three methods, the naive approach, the multiple shooting (MS) method [55] and our key frame loss method. The naive approach computes loss by the each time step difference between the ground truth trajectory and the estimated one. The MS splits the trajectory to multiple windows and compute the loss by defects at the end of each window. Multiple number of windows is tested.

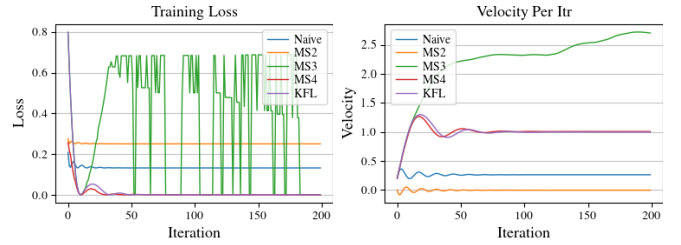


Fig. 16. Loss and velocity curve comparison during the training process of Naive approach (Naive), multiple shooting with 2 (MS2), 3 (MS3), 4 (MS4) windows, and our Key Frame Loss method (KFL). Only our KFL loss and MS4 could converge to the ground truth velocity (1m/s). Naive, MS2 and MS3 fail due to conflicted gradients.

The performance comparisons is in Figure 16. Only our KFL and MS4 could converge the velocity to the correct value (1m/s). All others fail due to conflicted gradients. We also test MS method with 5-9 windows. Although the loss curves are slightly bumpy, the velocity also converges to the correct value. To ensure the correct gradient direction, We suppose the number of shooting windows should be more than twice than the number of gaits (here is 3), which follows the Nyquist-Shannon sampling theorem. MS method samples discrete gradients on a continuous trajectory, and the sampling frequency should be more that the twice of the trajectory's frequency. However, the frequency should not be too high for noisy ground truth data, where the noise gradient may dominate the optimization. Our KFL splits the trajectory by 'gait' to increase the gradient sampling interval to overcome the observation noise.

## V. CONCLUSIONS

This paper proposed a R2S2R pipeline to identify the tensegrity robot and generate new locomotion policies. With a differentiable physics engine, the sim2real gap can be reduced by learning system parameters via a efficient gradient descent approach and the new polices can be generated effectively via symmetry reduction. These polices are extended to long trajectories, which are successfully transferred back to a real tensegrity robot. Since the cable length sensors may succumb to wear and tear, an adaptive simulator with more qualitative predictions are expected in the future.

## REFERENCES

- [1] S. Lessard, D. Castro, W. Asper, S. D. Chopra, L. B. Baltaxe-Admony, M. Teodorescu, V. SunSpiral, and A. Agogino, "A bio-inspired tensegrity manipulator with multi-dof, structurally compliant joints," in *2016 IEEE/RSJ International Conference on Intelligent Robots and Systems (IROS)*. IEEE, 2016, pp. 5515–5520.
- [2] A. P. Sabelhaus, L. J. van Vuuren, A. Joshi, E. Zhu, H. J. Garnier, K. A. Sover, J. Navarro, A. K. Agogino, and A. M. Agogino, "Design, simulation, and testing of a flexible actuated spine for quadruped robots," *arXiv preprint arXiv:1804.06527*, 2018.
- [3] M. Chen, J. Liu, and R. E. Skelton, "Design and control of tensegrity morphing airfoils," *Mechanics Research Communications*, vol. 103, p. 103480, 2020.
- [4] J. Bruce, A. P. Sabelhaus, Y. Chen, D. Lu, K. Morse, S. Milam, K. Caluwaerts, A. M. Agogino, and V. SunSpiral, "Superball: Exploring tensegrities for planetary probes," *12th International Symposium on Artificial Intelligence, Robotics, and Automation in Space (iSAIRAS)*, 2014.
- [5] NASA, "NASA Tensegrity Robotics Toolkit," Accessed 2020, <https://github.com/NASA-Tensegrity-Robotics-Toolkit/NTRTsim>.
- [6] C. Paul, F. Valero-Cuevas, and H. Lipson, "Design and control of tensegrity robots for locomotion," *IEEE Transactions on Robotics*, vol. 22, no. 5, pp. 944–957, Oct. 2006. [Online]. Available: <http://ieeexplore.ieee.org/document/1705585/>
- [7] S. Wittmeier, M. Jantsch, K. Dalamagkidis, *et al.*, "CALIPER: A universal robot simulation framework for tendon-driven robots," in *IROS*, 2011.
- [8] J. Friesen, "Tensegrity matlab objects," Accessed 2020, [https://github.com/Jfriesen222/Tensegrity\\_MATLAB\\_Objects](https://github.com/Jfriesen222/Tensegrity_MATLAB_Objects).
- [9] V. Tadiparthi, S.-C. Hsu, and R. Bhattacharya, "Stedy: Software for tensegrity dynamics," *Journal of Open Source Software*, vol. 4, no. 33, p. 1042, 2019.
- [10] R. Goyal, M. Chen, M. Majji, *et al.*, "Motes: Modeling of tensegrity structures," *Journal of Open Source Software*, vol. 4, no. 42, p. 1613, 2019.
- [11] K. Bousmalis and S. Levine, "Closing the simulation-to-reality gap for deep robotic learning (2019)," *Google AI Blog* <http://ai.googleblog.com/2017/10/closing-simulation-to-reality-gap-for.html>, 2019.
- [12] P. Martinez-Gonzalez, S. Oprea, A. Garcia-Garcia, A. Jover-Alvarez, S. Orts-Escolano, and J. Garcia-Rodriguez, "Unrealrox: an extremely photorealistic virtual reality environment for robotics simulations and synthetic data generation," *Virtual Reality*, vol. 24, no. 2, pp. 271–288, 2020.
- [13] J. K. Murthy, M. Macklin, F. Golemo, V. Voleti, L. Petrini, M. Weiss, B. Considine, J. Parent-Lévesque, K. Xie, K. Erleben, *et al.*, "gradsim: Differentiable simulation for system identification and visuomotor control," in *International Conference on Learning Representations*, 2020.
- [14] J. Collins, D. Howard, and J. Leitner, "Quantifying the reality gap in robotic manipulation tasks," in *2019 International Conference on Robotics and Automation (ICRA)*. IEEE, 2019, pp. 6706–6712.
- [15] F. Ramos, R. Possas, and D. Fox, "Bayessim: adaptive domain randomization via probabilistic inference for robotics simulators," in *Robotics: Science and Systems (RSS)*, 2019. [Online]. Available: <https://arxiv.org/abs/1906.01728>
- [16] F. Muratore, T. Gruner, F. Wiese, B. Belousov, M. Gienger, and J. Peters, "Neural posterior domain randomization," in *Conference on Robot Learning*. PMLR, 2022, pp. 1532–1542.
- [17] A. Zeng, S. Song, J. Lee, A. Rodriguez, and T. Funkhouser, "Tossing-bot: Learning to throw arbitrary objects with residual physics," *IEEE Transactions on Robotics*, vol. 36, no. 4, pp. 1307–1319, 2020.
- [18] V. Lim, H. Huang, L. Y. Chen, J. Wang, J. Ichnowski, D. Seita, M. Laskey, and K. Goldberg, "Real2sim2real: Self-supervised learning of physical single-step dynamic actions for planar robot casting," in *2022 International Conference on Robotics and Automation (ICRA)*. IEEE Press, 2022, p. 8282–8289.
- [19] M. A. Toussaint, K. R. Allen, K. A. Smith, and J. B. Tenenbaum, "Differentiable physics and stable modes for tool-use and manipulation planning," *Robotics: Science and Systems Foundation*, 2018.
- [20] E. Heiden, D. Millard, H. Zhang, and G. S. Sukhatme, "Interactive differentiable simulation," *arXiv preprint arXiv:1905.10706*, 2019.
- [21] E. Heiden, M. Macklin, Y. S. Narang, D. Fox, A. Garg, and F. Ramos, "DiSECT: A Differentiable Simulation Engine for Autonomous Robotic Cutting," in *Proceedings of Robotics: Science and Systems*, Virtual, July 2021.
- [22] Y. Qiao, J. Liang, V. Koltun, and M. Lin, "Differentiable simulation of soft multi-body systems," *Advances in Neural Information Processing Systems*, vol. 34, pp. 17 123–17 135, 2021.
- [23] S. Li, Z. Huang, T. Du, H. Su, J. B. Tenenbaum, and C. Gan, "Contact points discovery for soft-body manipulations with differentiable physics," *arXiv preprint arXiv:2205.02835*, 2022.
- [24] X. Lin, Z. Huang, Y. Li, J. B. Tenenbaum, D. Held, and C. Gan, "DiffSkill: Skill abstraction from differentiable physics for deformable object manipulations with tools," *arXiv preprint arXiv:2203.17275*, 2022.
- [25] M. Lutter, J. Silberbauer, J. Watson, and J. Peters, "A differentiable newton-euler algorithm for real-world robotics," *arXiv preprint arXiv:2110.12422*, 2021.
- [26] F. Liu, M. Li, J. Lu, E. Su, and M. C. Yip, "Parameter identification and motion control for articulated rigid body robots using differentiable position-based dynamics," *arXiv preprint arXiv:2201.05753*, 2022.
- [27] B. Plancher, S. M. Neuman, R. Ghosal, S. Kuindersma, and V. J. Reddi, "Grid: Gpu-accelerated rigid body dynamics with analytical gradients," in *2022 International Conference on Robotics and Automation (ICRA)*. IEEE, 2022, pp. 6253–6260.
- [28] T. Du, J. Hughes, S. Wah, W. Matusik, and D. Rus, "Underwater soft robot modeling and control with differentiable simulation," *IEEE Robotics and Automation Letters*, vol. 6, no. 3, pp. 4994–5001, 2021.
- [29] M. Bäcker, E. Knoop, and C. Schumacher, "Design and control of soft robots using differentiable simulation," *Current Robotics Reports*, pp. 1–11, 2021.
- [30] S. Chen, K. Werling, and C. K. Liu, "Real-time model predictive control and system identification using differentiable physics simulation," *arXiv preprint arXiv:2202.09834*, 2022.
- [31] W. Wang, S. Axelrod, and R. Gómez-Bombarelli, "Differentiable molecular simulations for control and learning," in *ICLR 2020 Workshop on Integration of Deep Neural Models and Differential Equations*, 2020. [Online]. Available: <https://openreview.net/forum?id=YDNzrQRsu>
- [32] K. Wang, M. Aanjaneya, and K. Bekris, "Sim2sim evaluation of a novel data-efficient differentiable physics engine for tensegrity robots," in *IEEE/RSJ International Conference on Intelligent Robots and Systems (IROS)*, 2021, pp. 1–8.
- [33] —, "A first principles approach for data-efficient system identification of spring-rod systems via differentiable physics engines," in *Proceedings of the 2nd Conference on Learning for Dynamics and Control*, ser. Proceedings of Machine Learning Research, A. M. Bayen, A. Jadbabaie, G. Pappas, P. A. Parrilo, B. Recht, C. Tomlin, and M. Zeilinger, Eds., vol. 120. PMLR, 10–11 Jun 2020, pp. 651–665.
- [34] —, "A recurrent differentiable engine for modeling tensegrity robots trainable with low-frequency data," in *2022 IEEE International Conference on Robotics and Automation (ICRA)*, 2022.
- [35] M. Zhang, X. Geng, J. Bruce, K. Caluwaerts, M. Vespignani, V. SunSpiral, P. Abbeel, and S. Levine, "Deep reinforcement learning for tensegrity robot locomotion," in *2017 IEEE International Conference on Robotics and Automation (ICRA)*. IEEE, 2017, pp. 634–641.
- [36] J. Luo, R. Edmunds, F. Rice, and A. M. Agogino, "Tensegrity robot locomotion under limited sensory inputs via deep reinforcement learning," in *2018 IEEE International Conference on Robotics and Automation (ICRA)*. IEEE, 2018, pp. 6260–6267.
- [37] D. Surovik, K. Wang, M. Vespignani, J. Bruce, and K. E. Bekris, "Adaptive Tensegrity Locomotion: Controlling a Compliant Icosahedron with Symmetry-Reduced Reinforcement Learning," *International Journal of Robotics Research (IJRR)*, 2019.
- [38] B. T. Mirletz, I.-W. Park, R. D. Quinn, and V. SunSpiral, "Towards bridging the reality gap between tensegrity simulation and robotic hardware," in *2015 IEEE/RSJ International Conference on Intelligent Robots and Systems (IROS)*. IEEE, 2015, pp. 5357–5363.
- [39] K. Caluwaerts, J. Despraz, A. İşçen, A. P. Sabelhaus, J. Bruce, B. Schrauwen, and V. SunSpiral, "Design and control of compliant tensegrity robots through simulation and hardware validation," *Journal of the royal society interface*, vol. 11, no. 98, p. 20140520, 2014.
- [40] A. Sethuraman and K. A. Skinner, "Towards sim2real for shipwreck detection in side scan sonar imagery," *3rd Workshop on Closing the Reality Gap in Sim2Real Transfer for Robotics*, 2022.
- [41] M. Navardi, P. Dixit, T. Manjunath, N. R. Waytowich, T. Mohsenin, and T. Oates, "Toward real-world implementation of deep reinforcement learning for vision-based autonomous drone navigation with mission," *UMBC Student Collection*, 2022.

- [42] A. Loquercio, E. Kaufmann, R. Ranftl, A. Dosovitskiy, V. Koltun, and D. Scaramuzza, "Deep drone racing: From simulation to reality with domain randomization," *IEEE Transactions on Robotics*, vol. 36, no. 1, pp. 1–14, 2019.
- [43] A. Sena, H. Kavianirad, S. Endo, E. Burdet, and S. Hirche, "The gap in functional electrical stimulation simulation," *3rd Workshop on Closing the Reality Gap in Sim2Real Transfer for Robotics*, 2022.
- [44] J. Jabbour, "Closing the sim-to-real gap for ultra-low-cost, resource-constrained, quadruped robot platforms," *3rd Workshop on Closing the Reality Gap in Sim2Real Transfer for Robotics*, 2022.
- [45] W. Huang, X. Huang, C. Majidi, and M. K. Jawed, "Dynamic simulation of articulated soft robots," *Nature communications*, vol. 11, no. 1, pp. 1–9, 2020.
- [46] X. Huang, W. Huang, Z. Patterson, Z. Ren, M. K. Jawed, and C. Majidi, "Numerical simulation of an untethered omni-directional star-shaped swimming robot," in *2021 IEEE International Conference on Robotics and Automation (ICRA)*. IEEE, 2021, pp. 11 884–11 890.
- [47] N. N. Goldberg, X. Huang, C. Majidi, A. Novelia, O. M. O'Reilly, D. A. Paley, and W. L. Scott, "On planar discrete elastic rod models for the locomotion of soft robots," *Soft robotics*, vol. 6, no. 5, pp. 595–610, 2019.
- [48] B. Wen, W. Lian, K. Bekris, and S. Schaal, "Catgrasp: Learning category-level task-relevant grasping in clutter from simulation," in *2022 International Conference on Robotics and Automation (ICRA)*. IEEE, 2022, pp. 6401–6408.
- [49] J. Bruce, K. Caluwaerts, A. Iscen, A. P. Sabelhaus, and V. SunSpiral, "Design and evolution of a modular tensegrity robot platform," in *2014 IEEE International Conference on Robotics and Automation (ICRA)*. IEEE, 2014, pp. 3483–3489.
- [50] A. Moldagalieva, D. Fadeyev, A. Kuzdeuov, V. Khan, B. Alimzhanov, and H. A. Varol, "Computer vision-based pose estimation of tensegrity robots using fiducial markers," in *2019 IEEE/SICE International Symposium on System Integration (SII)*. IEEE, 2019, pp. 478–483.
- [51] S. Lu, W. R. J. III, K. Wang, X. Huang, J. Booth, R. Kramer-Bottiglio, and K. Bekris, "6n-dof pose tracking for tensegrity robots," 2022.
- [52] M. A. Fischler and R. C. Bolles, "Random sample consensus: a paradigm for model fitting with applications to image analysis and automated cartography," *Communications of the ACM*, vol. 24, no. 6, pp. 381–395, 1981.
- [53] K. Werling, D. Omens, J. Lee, I. Exarchos, and C. K. Liu, "Fast and feature-complete differentiable physics engine for articulated rigid bodies with contact constraints," in *Robotics: Science and Systems*, 2021.
- [54] Pytorch, "Pytorch Detach Method," Accessed 2022, <https://pytorch.org/docs/stable/generated/torch.Tensor.detach.html>.
- [55] E. Heiden, C. E. Denniston, D. Millard, F. Ramos, and G. S. Sukhatme, "Probabilistic inference of simulation parameters via parallel differentiable simulation," *International Conference on Robotics and Automation (ICRA)*, 2022.
- [56] D. Surovik, J. Bruce, K. Wang, M. Vespignani, and K. E. Bekris, "Any-axis tensegrity rolling via bootstrapped learning and symmetry reduction," in *International Symposium on Experimental Robotics (ISER)*, Buenos Aires, Argentina, 11/2018 2018.
- [57] W. R. Johnson, J. Booth, and R. Kramer-Bottiglio, "Integrated sensing in robotic skin modules," in *2021 IEEE Sensors*. IEEE, 2021, pp. 1–4.



## APPENDIX

### VI. DETACH METHOD ON FRICTION LEARNING

The detachment approach can also be applied to friction learning, which is shown in Algorithm 2. We detach  $\Delta v$  because friction force is a passive force. We add term  $-\Delta p_f + \Delta p_f.detach()$  to pass gradient to  $\mu$  in case only static friction.

#### Algorithm 2 Detach Method in Friction Computation

---

```

 $v'_{t+1} = v_t + F/m\Delta t$ 
 $\Delta v = -v'_{t+1}.detach()$ 
 $\Delta p_f = \mu N \Delta t / m$ 
if  $|\Delta v| > \Delta p_f$  then  $\Delta v = \Delta v * \Delta p_f / |\Delta v|$ 
else  $\Delta v = \Delta v - \Delta p_f + \Delta p_f.detach()$ 
end if
 $v_{t+1} = v_t + F/m\Delta t + \Delta v$ 
 $x_{t+1} = x_t + v_{t+1}\Delta t$ 

```

---

In general, we suggest to apply the "detach" method to clamping contacts of all actuated objects. However, this method should not be applied to objects whose movement only relies on these passive contact forces, e.g. the billiard. The philosophy is that we keep the "trending" gradient from the small actuation force even if the object can't move. This avoids the gradient discontinuities between clamping contact and separating contact.

### VII. CONTACT GRADIENTS WITH/WITHOUT "DETACH"

We bring the box problem, pulling a box to the target position in 200 time steps, to evaluate Algorithm 2. The pulling force  $F$  is known and the ground friction coefficient  $\mu$  is to be estimated. We take the MSE of box position and target position as loss function.

The initial  $\mu$  is 1 and box can't be moved with such large friction. Our detach method can generate correct negative gradient to reduce  $\mu$  and the loss. However, without our method, the gradient is always zero and the loss curve never goes down.

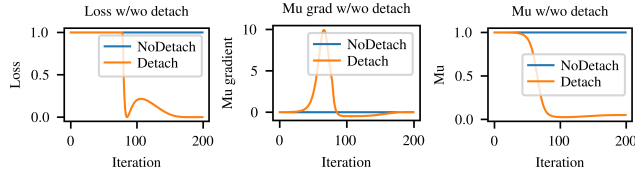


Fig. 17. The box pulling problem shows the detaching method can get correct gradient to reduce the friction coefficient  $\mu$ . Otherwise, zero gradients would happen on optimization of  $\mu$ .

Finally, we take the billiards problem, applying  $F$  on ball  $A$  and aiming the ball  $B$  to reach a target position in 500 timesteps, to evaluate the detaching philosophy - only detach actuated object. The loss is the mean MSE of  $B$ 's position and target position.

We compare the differences between detaching both  $A, B$  and detaching  $A$  only. As we suggested, we should only detach the actuated object  $A$ 's contact response. We shouldn't

detach  $B$ 's contact response, Because  $B$  is only affected by the passive contact forces. The result in Figure 18 shows that detaching both  $A$  and  $B$  could get zero gradient on  $F$  and no change in  $F$  and loss. However, if we only detach the actuated object  $A$ , we can still get correct gradient direction and escape the saddle point.

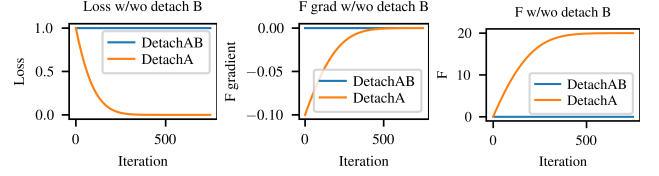


Fig. 18. The billiards problem shows that only detaching the actuated object  $A$  can get the correct gradient on actuation force  $F$  to reduce the loss. Detaching the passive moved object  $B$  will isolate  $B$  from gradient passing, which result to zero gradients on  $F$ .

### VIII. KEY FRAME LOSS

To get the key frames, we split the trajectory to gaits for convex segmentation as shown in Figure 19. In each gait, each cable follows only one of the controls: retracted, kept or released. These controls push or pull the end cap to form a convex trajectory segment. This avoids the zig-zag trajectory which lead to contradicted gradients shown in the Figure 8.

The key frame (KF) is the last time step of each gait. Let's consider a simple example trajectory with 3 gaits as shown in Figure 19. Both ground truth (red) and engine predicted trajectory are split into two three gaits. The corresponding gaits are remapped and the key frame (KF) are the last time frame of their intersections. The Key Frame Loss (KFL) is the system difference, e.g. the positions difference of the end caps, at these time frames.

We select the last time step because 1) The noisy ground truth observation around the start of each gait may lead to worse fitting as shown in Figure 7; 2) Since the system state relies on the preceding system states, the states starting each gait are still different; 3) The gait transition point is where one gait is finished. However, whether a gait is done if by the measurement from noisy cable length sensors. This would lead to earlier or later transition, which shows as small gaps in Figure 19 after alignment.

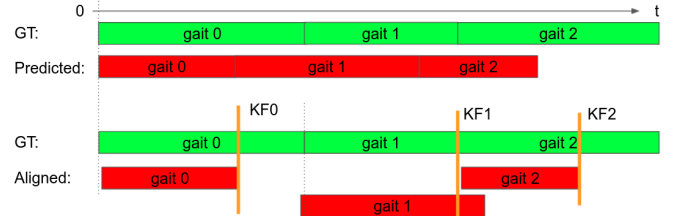


Fig. 19. Up: The ground truth (GT) and engine predicted (Predicted) trajectory are split to three gaits, based on the control. Down: The gaits are aligned at the starting points and their key frames (KF0, KF1, KF2) are the last time frame of each intersection. The predicted trajectory takes less time in gait 0 and 2, but more time in 1. This leads to contradicted gradient direction.

However, Losses from different gaits may still have contradicted gradients. In Figure 19, the predicted trajectory takes less time for gait 0 and 2, but takes more time for gait 1.

These may confuse the optimizer whether to speed up or slow down. Possible reasons for these are: 1) The ground truth time stamp is noisy due to the sensor limitation; 2) noisy cable length sensor reading leads to early or later gait transition; 3) the starting states are not perfectly aligned; 4) gaps between simplified physics engine and complex real robot.

We adopt a mask filter the contradicted gradients among these gaits. The rule of thumb is that the identified engine should execute same gaits on the robot with similar time and behavior. Then we take the whole trajectory execution time as an indicator to filter out those opposite gradients. In Figure 19, since the predicted trajectory takes shorter time than the ground truth. We only consider key frame losses of gait 0 and gait 2 to slow down the engine, and ignore that of gait 1.